

# Heterogeneous integration of amorphous silicon carbide on thin film lithium niobate

Zizheng Li,<sup>1</sup> Naresh Sharma,<sup>1</sup> Bruno Lopez-Rodriguez,<sup>1</sup> Roald van der Kolk,<sup>1</sup> Thomas Scholte,<sup>1</sup> Hugo Voncken,<sup>1</sup> Jasper van der Boom,<sup>1</sup> Simon Gröblacher,<sup>2</sup> and Iman Esmaeil Zadeh<sup>1</sup>

<sup>1</sup>*Department of Imaging Physics (ImPhys), Faculty of Applied Sciences, Delft University of Technology, Delft 2628 CJ, The Netherlands*

<sup>2</sup>*Department of Quantum Nanoscience, Faculty of Applied Sciences, Delft University of Technology, Delft 2628 CJ, The Netherlands*

(\*Electronic mail: z.li-1@tudelft.nl)

(Dated: 15 July 2024)

In the past decade, lithium niobate (LiNbO<sub>3</sub> or LN) photonics, thanks to its heat-free and fast electro-optical modulation, second-order non-linearities and low loss, has been extensively investigated. Despite numerous demonstrations of high-performance LN photonics, processing lithium niobate remains challenging and suffers from incompatibilities with standard complementary metal-oxide semiconductor (CMOS) fabrication lines, limiting its scalability. Silicon carbide (SiC) is an emerging material platform with a high refractive index, a large non-linear Kerr coefficient, and a promising candidate for heterogeneous integration with LN photonics. Current approaches of SiC/LN integration require transfer-bonding techniques, which are time-consuming, expensive, and lack precision in layer thickness. Here we show that amorphous silicon carbide (a-SiC), deposited using inductively coupled plasma enhanced chemical vapor deposition (ICPCVD) at low temperatures (< 165°C), can be conveniently integrated with LiNbO<sub>3</sub> and processed to form high-performance photonics. Most importantly, the fabrication only involves a standard, silicon-compatible, reactive ion etching step and leaves the LiNbO<sub>3</sub> intact, hence its compatibility with standard foundry processes. As a proof-of-principle, we fabricated waveguides and ring resonators on the developed a-SiC/LN platform and achieved intrinsic quality factors higher than  $1.06 \times 10^5$  and resonance electro-optic tunability of 3.4 pm/V with 3 mm tuning length. We showcase the possibility of dense integration by fabricating and testing ring resonators with 40 μm radius without a noticeable loss penalty. Our platform offers a CMOS-compatible and scalable approach for implementation of future fast electro-optic modulators and reconfigurable photonic circuits as well as nonlinear processes which can benefit from involving both second and third-order nonlinearities.

## I. INTRODUCTION

Lithium niobate (LiNbO<sub>3</sub> or LN) is a material platform widely utilized in telecommunication as electro-optical modulators, tunable photonic integrated circuits (PICs), and a variety of other applications. Lithium niobate is known for its remarkable properties such as broad transparency window,<sup>1,2</sup> low loss,<sup>3–6</sup> high second order nonlinearity coefficient,<sup>7–10</sup> strong Pockels effect,<sup>11–13</sup> good physical and chemical stability.<sup>14</sup> The platform has been employed in studies in optical communications,<sup>13,15–17</sup> microwave photonics,<sup>13,18</sup> and quantum computing<sup>19–23</sup>.

To fabricate LiNbO<sub>3</sub> PICs, approaches ranging from titanium in-diffusion,<sup>24,25</sup> proton exchange,<sup>26,27</sup> direct etching,<sup>5,28,29</sup> dielectric rib-loading circuits,<sup>30,31</sup> wafer bonding<sup>17,32</sup> and plasmonic waveguides<sup>33</sup> have been successfully demonstrated. The first two methods use bulk LN substrate and locally alter the refractive index in a certain volume to create a small index contrast with respect to the substrate and cladding. These methods can only create weak confinement and hence result in high bending losses and, moreover, they have contamination issues and the fabrication processes are time consuming<sup>34</sup>. In contrast, direct etched waveguides and rib-loading circuits based on thin film lithium niobate (TFLN) substrate can overcome these challenges. With the smart-cut technology, a LiNbO<sub>3</sub> thin film with a thickness less than 1 μm can be transferred and bonded to an acceptor substrate, which forms the lithium niobate

on insulator substrate.<sup>35,36</sup> Dry etching methods such as reactive ion etching or argon milling etching are commonly chosen to define the PICs on these TFLN films,<sup>29,36,37</sup> and have already proven high quality and ultralow loss photonic devices.<sup>6</sup> However, direct LN etching also has a number of disadvantages: low selectivity between LN and etching masks, non-vertical sidewall angle (typically around 60°), re-deposition of etching byproducts such as LiF which is difficult to be removed at low temperature are examples of these issues. In addition, and crucially, etching of LN is not compatible with complementary metal oxide semiconductor (CMOS) fabrication lines, since the etching byproducts and lithium out-diffusion are considered as contamination<sup>25,38</sup>. All of these problems are limiting the possibilities in design and hampering the way towards large scale fabrication and mass production.

Hybrid integration of rib-loading waveguides with TFLN offers another feasible path to fabricate compact, low-loss, and scalable PICs<sup>31</sup>. The integration can be realized using two different schemes, namely, transfer/bond of a pre-fabricated PIC wafer/chip onto a TFLN substrate, or monolithical deposition of a thin film directly on the TFLN substrate followed by fabrication of the rib-loading waveguides on this layer. Regarding the former, various techniques are used to construct the heterogeneous platforms<sup>17,32,39–41</sup>. Challenges from transfer bonding process include layer-to-layer misalignment, thermal stress mismatch, and surface non-uniformity and roughness.<sup>42–45</sup> To circumvent the mentioned disadvan-

tages associated with transfer bonding, delicate and costly procedures such as ion-slicing and multiple rounds of chemical mechanical polishing (CMP) have been utilized, which adds further complexities and limitations. In contrast, monolithic deposition and etching scheme is a comparatively more stable and convenient option. Various materials, ranging from amorphous silicon (a-Si) to  $\text{Ta}_2\text{O}_5$  and  $\text{TiO}_2$  have been deposited on TFLN and heterogeneous PIC devices on these platforms have been demonstrated.<sup>46–50</sup> Among them, a-Si on TFLN platform offers the merits of small footprint and large thermal-optics tunability but suffers from narrow bandgap and weak mode interaction with  $\text{LiNbO}_3$ , while the others, in addition to similar issues as a-Si, also suffer from incompatibility with CMOS foundries or immature fabrication process.

Amorphous silicon carbide (a-SiC) has recently emerged as a promising option for PICs thanks to its strong optical confinement, wide transparent window, high thermo-optical coefficient, low loss, and high Kerr nonlinear coefficient<sup>51–57</sup>. Compared to the different polytypes of crystalline silicon carbide used in photonics (3C-SiC, 4H-SiC or 6H-SiC), amorphous silicon carbide material properties can be easily tuned, allows for precise control in layer thickness and has ten times higher Kerr nonlinear coefficient, providing broader possibilities in the field of nonlinear optics. Notably, a-SiC can be deposited at low temperature ( $\leq 150^\circ\text{C}$ ) using inductively coupled plasma chemical vapour deposition (ICPCVD) without sacrificing the film quality, which indicates that lift-off of a-SiC films and monolithic integration of devices with different thicknesses and on different platforms are possible.<sup>51</sup> Essentially, the a-SiC rib-loading scheme can fulfill all the merits expected for the heterogeneous integration with TFLN, which enhances a multitude of possible applications, including compact and ultra-fast optical modulators, high density and low loss passive PICs, second order nonlinearity and Kerr nonlinearity, high efficiency on-chip spontaneous down conversion and deterministic integration of single photon sources for quantum photonic applications<sup>58</sup>.

In this paper, for the first time a-SiC/TFLN heterogeneous photonic integration is proposed and investigated. Based on an optimized ICPCVD a-SiC on TFLN fabrication processes, we designed, fabricated and characterized on-chip photonic devices and analyzed their performance. Our results demonstrate the high potentials of the proposed platform in future PIC applications.

## II. METHODS AND RESULTS

### A. Fabrication

We fabricated the a-SiC rib-loading PICs on the LNOI substrates (NanoLN), which consists of 500 nm TFLN on  $2\mu\text{m}$  buried  $\text{SiO}_2$  layer on  $300\mu\text{m}$  Si substrate. As shown in Fig.1(a), 260 nm a-SiC deposition was done via ICPCVD in Oxford PlasmaPro 100 with mixed precursors of  $\text{SiH}_4$  and  $\text{CH}_4$  at a table temperature of  $150^\circ\text{C}$ . Argon (Ar) flow was chosen as the deposition environment. The chamber pressure is set to 2 mTorr. It is known that high temperature

processes can potentially cause problems, such as unwanted diffusion, non-releasable thermal stress or thermal expansion mismatch, which renders the fabrication process CMOS incompatible. The low-temperature deposited ICPCVD a-SiC film mitigates these challenges, and allows monolithic integration of PICs with different thicknesses on TFLN<sup>51</sup>. After a-SiC deposition, ellipsometry measurements were performed (Woollam M-2000 spectroscopic ellipsometer) to find out the refractive index of a-SiC. The real and imaginary index ( $n$  and  $k$ ) results are shown in Fig.1(c). Around 1550 nm, wavelength of interest in this work, the complex refractive index is found to be  $2.73 + i8.4 \times 10^{-5}$  (fitted by B-spline expanded Cauchy model with Cody-Lorentz oscillators<sup>59</sup>). To determine the surface roughness, which places significant impact on the optical waveguide loss, we conducted an atomic force microscopy (AFM) measurement in a  $4\mu\text{m} \times 4\mu\text{m}$  region on the top surface of a-SiC film (shown in Fig.1(b)). We obtained an root-mean-square (RMS) value of  $(0.45 \pm 0.06)$  nm, indicating good deposition quality and surface flatness.

Fabrication flow for electro-optically tunable devices is shown in Fig.1(d). To fabricate the PIC waveguides, electron beam lithography (EBL) resist (CSAR 62) was spin-coated and baked at  $160^\circ\text{C}$  for 2 minutes. The rib-loading PIC pattern was defined on the resist layer by EBL exposure (Raith 100-kV EBPG-5200), and after development it was transferred to the a-SiC layer by reactive-ion etching (RIE, Sentech Etchlab 200) using a gas mixture of  $\text{SF}_6$  and  $\text{O}_2$ . The etching time was carefully controlled to prevent over-etching. The electrodes for electro-optics are fabricated by standard lift-off process. 10 nm chromium (Cr) and 450 nm gold (Au) are deposited by electron beam evaporation on the openings, pre-defined by another EBL step, followed by the lift-off process in resist stripper (PRS-3000). Since ICPCVD  $\text{SiO}_2$  can also be deposited at low temperature ( $150^\circ\text{C}$ ), so that compatible to standard lift-off process, the same EBL/lift-off procedure is employed to fabricate the  $\text{SiO}_2$  cladding. The  $\text{SiO}_2$  cladding covers all the optical devices but leaving the Au electrodes exposed for the convenience of wire-bonding. Following each EBL exposure, the resist was reflowed at  $130^\circ\text{C}$  for one minute after development, in order to enhance the etching aspect-ratio and reduce the sidewall roughness. It is essential to further clean the resist residuals using oxygen plasma after every chemical lift-off process, to maintain the surface roughness given by ICPCVD deposition and reduce optical scattering brought by remaining particles on the surface. A stitched optical microscopy image of fabricated devices is shown in Fig.1(e), with an inset zooming in on the region of the waveguide sandwiched between the Au electrodes.

### B. Design and Simulation

In the heterogeneous a-SiC/TFLN platform, optical modes are confined and propagated around the rib-loading a-SiC waveguides, in a way that only fundamental TE/TM modes are supported and the mode overlapping fraction with the two materials can be engineered by altering the waveguide width. As illustrated in Fig.2(a), the racetrack ring resonator con-

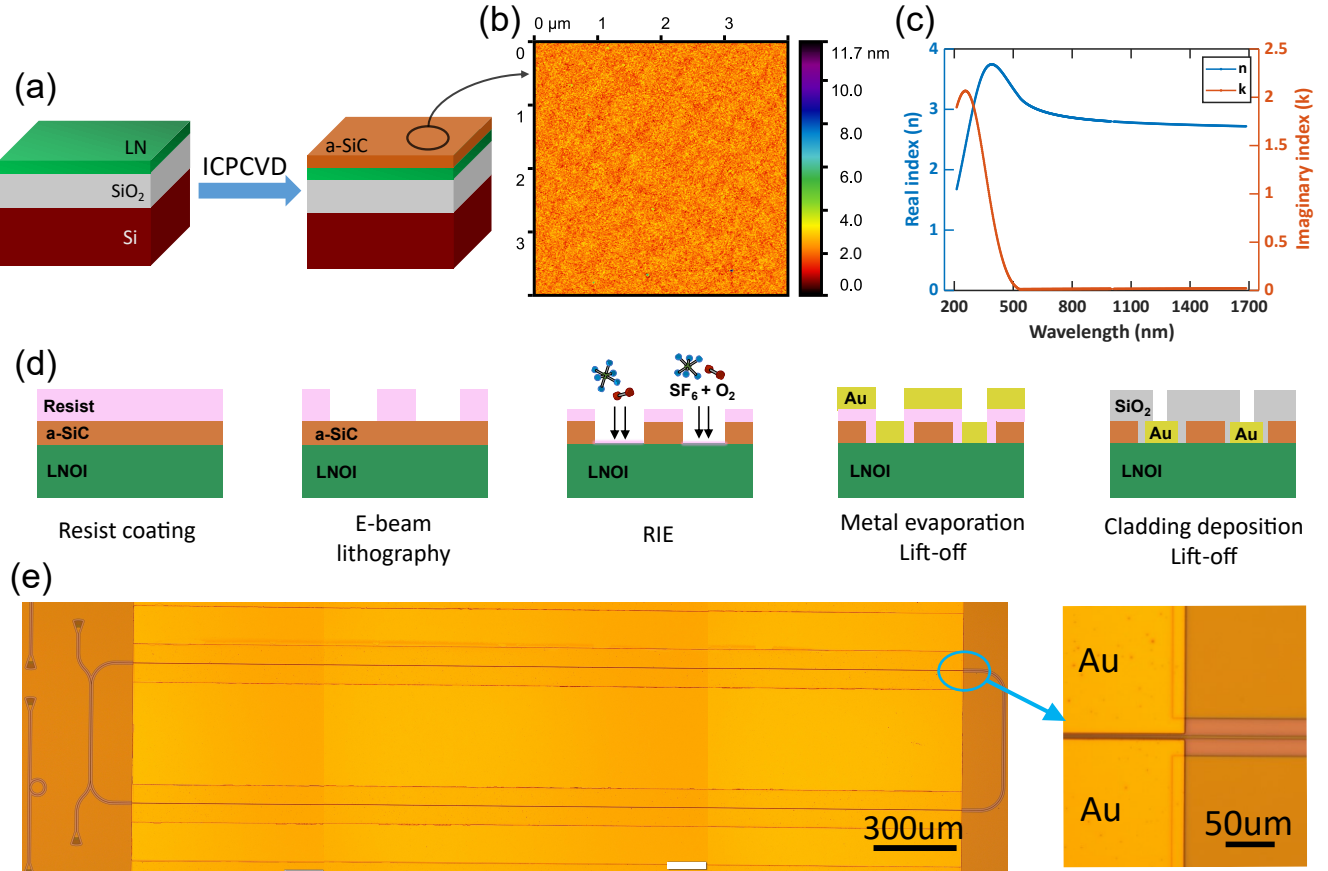


FIG. 1. (a) a-SiC thin film deposition on LNOI substrate. (b) AFM measurement result on a-SiC surface. (c) Real and imaginary refractive index ( $n$  and  $k$ ) of the a-SiC film. (d) Fabrication flow of electro-optical tunable a-SiC/TFLN devices. (e) Microscopy image (stitched) of fabricated racetrack ring resonator, with the inset: region of the waveguide between two Au electrodes.

sists of normal waveguides (width  $w_1 = 800$  nm, height  $h = 260$  nm), adiabatic tapers and narrow waveguides (width  $w_2 = 400$  nm, height  $h = 260$  nm). Here we define the mode overlapping fraction in the LN layer as  $\Gamma_{LN}$ , denoting the effective percentage of mode intensity distribution and interaction with the material LN. In the standard waveguides, optical modes are relatively strongly confined by the a-SiC waveguides, and the mode overlapping fraction of the fundamental modes are  $\Gamma_{LN-TE} = 33.65\%$  and  $\Gamma_{LN-TM} = 57.04\%$ , as shown in Fig.2(b) and (c). Correspondingly, the confinement becomes weaker when the waveguides width is tapered down, which results in  $\Gamma_{LN-TE} = 66.03\%$  and  $\Gamma_{LN-TM} = 68.11\%$  respectively in the narrow waveguides (shown in Fig.2(d) and (e)). In both cases, the waveguides dimensions are designed to ensure that only fundamental modes are supported. The standard waveguides are used for propagation and sharp bendings, utilizing the strong confinement property, while the narrow waveguides can be used for larger interaction between propagation modes and LN layer to enhance EO tuning efficiency. The longer arms of the racetrack ring, marked in Fig.2(a) with  $L_2 = 3000 \mu\text{m}$ , are aligned perpendicular to the LN crystal z-axis

(marked at the left-bottom corners in Fig.2(b)-(e)) to excite the Pockels effect with the largest EO coefficient  $r_{33} = 30.9$  pm/V<sup>38</sup>. The mode distributions and overlapping fractions are simulated by finite difference eigenmode solver (MODE, Ansys Lumerical) based on the material properties mentioned in the previous section, taking the refractive index of LN as  $n_e = 2.13$  and  $n_o = 2.21$  around  $1550$  nm<sup>2,25</sup>. Mesh grid size is chosen close to the lithography resolution and convergence test is performed with perfect matching layer (PML) boundary conditions. Adiabatic tapers with a length of  $L_3 = 100 \mu\text{m}$  are adopted to convert the propagation modes between the standard and narrow waveguides. The gap between the bus and ring waveguides is set to  $400$  nm, and accompanied with the coupling length (shorter arm)  $L_1 = 500 \mu\text{m}$  the racetrack ring resonator is brought to critical coupling regime. At the both ends of the bus waveguide, there are two apodized grating couplers enabling efficient in-and-out fiber coupling.

For EO tuning, we use G-S-G electrodes configuration to minimize the tuning length and device footprint, as depicted in Fig.2(a). In order to optimize the tuning efficiency and electrodes parameters, the Charge Transport (CHARGE, An-

sys Lumerical) and Finite Element EigenMode (FEEM, Ansys Lumerical) simulations are implemented. Except for the mentioned waveguides geometry, the gap  $g$  between the ground and signal is another vital variable that influences the EO tuning performance. There is an inevitable trade-off between higher EO tuning efficiency (smaller  $g$ ) and low propagation loss (larger  $g$ ), which suggests that a balanced point of  $g$  needs to be engineered. The propagation loss in the simulations is obtained from the imaginary part of the mode effective index  $k$ . In the plane where extraordinary LiNbO<sub>3</sub> crystal axis is parallel aligned to the applied electric field  $E$  (this work focus on this situation mainly), the EO tuning efficiency can be evaluated by the half-wave voltage-length product  $V_\pi \cdot L$  as:

$$V_\pi \cdot L = \frac{\lambda d}{2n_e^3 r_{33}}$$

where  $d$  is the distance between the anode and cathode given the electric field  $E = V/d$ .<sup>32,38,41</sup>

Several sets of parameters are compared for both TE and TM modes:  $w_1 = 800$  nm,  $w_2 = 400$  nm corresponding to the standard waveguide width and narrow waveguide width; signal-ground electrodes gap  $g_1 = 3.8 \mu\text{m}$ ,  $g_2 = 4.8 \mu\text{m}$ ,  $g_3 = 4.4 \mu\text{m}$ ,  $g_4 = 6 \mu\text{m}$ . Fig.2(f) shows the effective index change corresponding to the voltage change applied to the signal pad. Clear polarization dependence can be seen, that for fundamental TE mode the effective index change slope is larger than that of the TM mode. This is due to the difference of EO coefficients along the ordinary and extraordinary axis ( $r_{33} = 30.9$  pm/V,  $r_{13} = 9.6$  pm/V). The narrowed waveguide structure has a larger fraction of the optical mode concentrated in the LN layer, resulting in larger index changing slopes. Regarding the propagation losses compared in Fig.2(g), TE polarized modes, for a given gap, have lower losses. At the focused wavelength of 1550 nm, the absorption from the waveguide materials can be neglected. Consequently, the metal absorption caused by the Au electrodes is the primary contribution to the total propagation loss. From Fig.2(g), it is concluded that for normal waveguides, the metal absorption can be neglected (0.005 dB/cm) when  $g \geq 4.8 \mu\text{m}$ , while for narrow waveguides,  $g \geq 6 \mu\text{m}$  leads to a relatively larger loss (0.035 dB/cm). Half-wave voltage-length production is simulated and summarized in Fig.2(h). Considering the results in Fig.2(f)-(h), two preferable balanced combinations for TE mode can be found: for normal waveguides  $w_1 = 800$  nm,  $g_1 = 4.8 \mu\text{m}$ ,  $V_\pi \cdot L = 8.8$  V · cm; for narrow waveguides  $w_2 = 400$  nm,  $g_4 = 6 \mu\text{m}$ ,  $V_\pi \cdot L = 4.7$  V · cm, respectively. It allows sharp bends hence dense integration (strong confinement in the normal waveguides) and high electro-optical tunability (weak confinement in the narrow waveguides) on the same chip at the same time. To show the principle while eliminate the potential impact of metal absorption losses, we choose the normal waveguides design to characterize the passive and active response of the devices.

### C. Characterization of passive optical devices

Thin film quality and waveguide propagation loss were characterized using ring resonator with intrinsic quality factor  $Q_i$ ,<sup>51</sup> which is defined as:

$$Q_i = \frac{2Q_L}{1 + \sqrt{T}} = \frac{2\lambda_0}{FWHM(1 + \sqrt{T})}$$

where  $Q_L$  is the loaded quality factor,  $\lambda_0$  is the resonance wavelength,  $FWHM$  represents the full width half maximum of the resonance dip, and  $T$  is the on-resonance transmission. To extract the propagation loss from the intrinsic quality factor, we calculate loss  $\alpha$  as:

$$\alpha [\text{dB/cm}] = 10 \lg e \left( \frac{2\pi n_g}{Q_i \lambda_0} \right)$$

where the group index  $n_g$  is derived from free spectral range (FSR) of the optical cavity:

$$n_g = \frac{\lambda_0^2}{L_{total} \cdot FSR} = \frac{\lambda_0^2}{2(\pi R + L_2 + L_1) \cdot FSR}$$

in which  $L_{Total}$  represents the total length of the ring. The  $FSR$  can be obtained from the resonance spectra shown in Fig.3(a) and (b). In comparison to the simulation results mentioned in the previous section, for a ring consisting of normal waveguides (260 nm × 800nm), the simulated group indices for TE and TM modes are  $n_{gTE} = 2.738$  and  $n_{gTM} = 2.614$  at 1550 nm, corresponding to  $FSR$  of 113 pm and 118 pm respectively, which are in good agreement with the experimental results. Single resonance peaks acquired from the TE and TM spectra are fitted by the Lorentzian function (Fig.3(c) and (d)), showing  $FWHM$  of 22.38 pm for TE mode and 34.78 pm for TM mode, respectively. The calculated intrinsic quality factor for TE mode is 106,673, denoting a propagation loss of 4.48 dB/cm.

Ring resonators with different bending radii are fabricated and measured to analyze the influence of bending loss. Here, the gap between ring and bus waveguide is not critical, as the only focus is on the change of  $FWHM$  representing the variation in loss, regardless it is in the under-coupling or over-coupling regime. The Lorentzian fitting of the resonance dips from different rings are brought together in Fig.2(f) for comparison, in which one can see when decreasing the bending radius the  $FWHM$  does not change until  $R=40\mu\text{m}$ , while the  $FWHM$  becomes much wider from  $R=40\mu\text{m}$  to  $R=30\mu\text{m}$ . It is inferred that the bending loss can be neglected for  $R \geq 40\mu\text{m}$ , which enables denser integration compared with SiN rib-loading waveguides. Nevertheless, in the following context that we discuss electro-optics tuning, the bending radius of racetrack ring resonators is kept to 120  $\mu\text{m}$ , completely ruling out any bending losses.

### D. Characterization of EO tunability

The electro-optics response of the a-SiC/LN platform is characterized and analyzed. Fig.4(a) depicts the characterization setup, starting from a tunable laser (Photonics

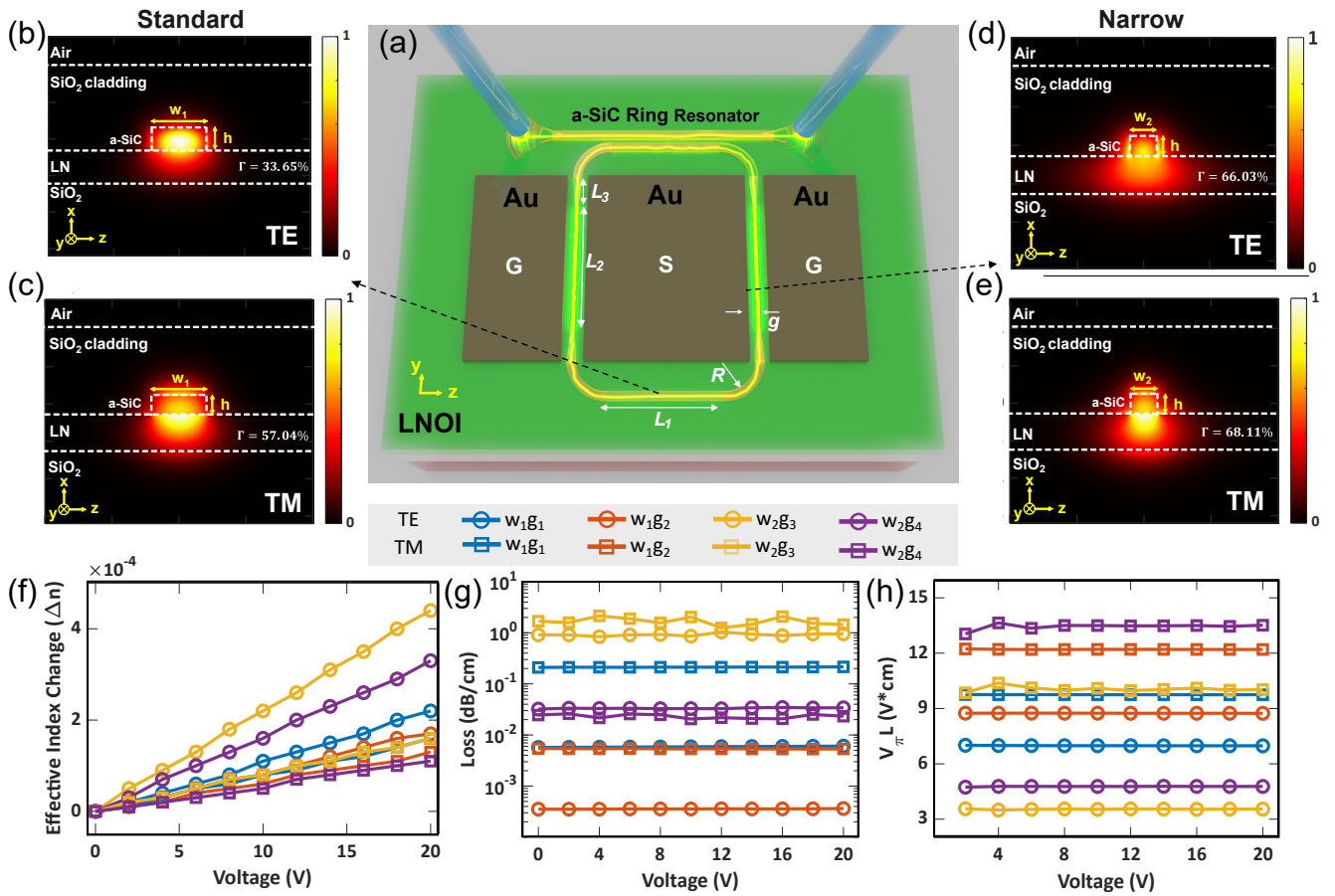


FIG. 2. (a) Schematic of the electro-optical tunable racetrack ring resonator. Mode distribution and mode-LN overlapping fraction of fundamental (b) TE and (c) TM modes in normal waveguides. (d) TE and (e) TM modes distribution with overlapping fraction in tapered down waveguides. (f) Effective index change, (g) propagation loss, and (h) half-wave voltage-length product with respect of applied voltages. (f)-(h) share the same legends, in which  $w_1 = 800$  nm,  $w_2 = 400$  nm,  $g_1 = 3.8$   $\mu\text{m}$ ,  $g_2 = 4.8$   $\mu\text{m}$ ,  $g_3 = 4.4$   $\mu\text{m}$ ,  $g_4 = 6$   $\mu\text{m}$ ,  $h = 260$  nm, and round markers represent TE mode while square markers represent TM mode.

TUNICS-PRI 3642 HE 15), the light passes through a paddle polarization controller and a free-space polarizer (Thorlabs FBR-LPNIR). The free-space polarizer is used to select specific polarizations, while the paddle polarization controller aligns the input light to the selected polarization. The polarized light is then coupled by a polarization maintaining fiber into the a-SiC/LN device by the on-chip apodized grating coupler. The output light is coupled out from another apodized grating coupler and collected by an optical powermeter (Newport 818-NR). To measure the electro-optics response, the sample is mounted on a printed circuit board (PCB), shown in Fig.4(b). Afterwards, the on-chip Au electrodes are wire-bonded to the PCB (Fig.4(c)). A power supply is used to generate DC voltage signals, of which the ground and output ports are connected to the pads on PCB by probes.

On the proposed heterogeneous a-SiC on TFLN platform, direct current (DC) driven Pockels effect is investigated to quantify the platform's tunability performance. Shown in the diagram in Fig.2(a), the racetrack ring resonator with Au electrodes is in push-pull configuration, with normal waveguides dimensions (260 nm  $\times$  800 nm) and gap  $g = 4.8$   $\mu\text{m}$ . Funda-

mental TE and TM modes are excited and characterized when voltage sweeping is performed on the Au electrodes, shown in Fig.4(d) and (e). The center wavelengths of the resonance dips are extracted and plotted in Fig.4(f) and (g), together with linear fitted curves that represents EO tuning trends. Nonlinear change of EO coefficient can be observed, due to the DC bias drift of LiNbO<sub>3</sub> crystal happening during the long engaging time of wavelength sweeping for every voltage level<sup>60–62</sup>. Based on the fitted EO response curves, the resonance tunability of 3.4 pm/V and 1.2 pm/V is realized, for TE mode and TM mode respectively. We calculated the half-wave voltage-length product and obtained 9.79 V·cm for the TE mode and 27.5 V·cm for the TM mode..

The difference between the simulation results and experimental results is believed to be related to the misalignment between racetrack longer arms and the LN crystal axis, also the mode profile is solved within the cross-section of the waveguides and considered to be consistently propagated in the third axis.

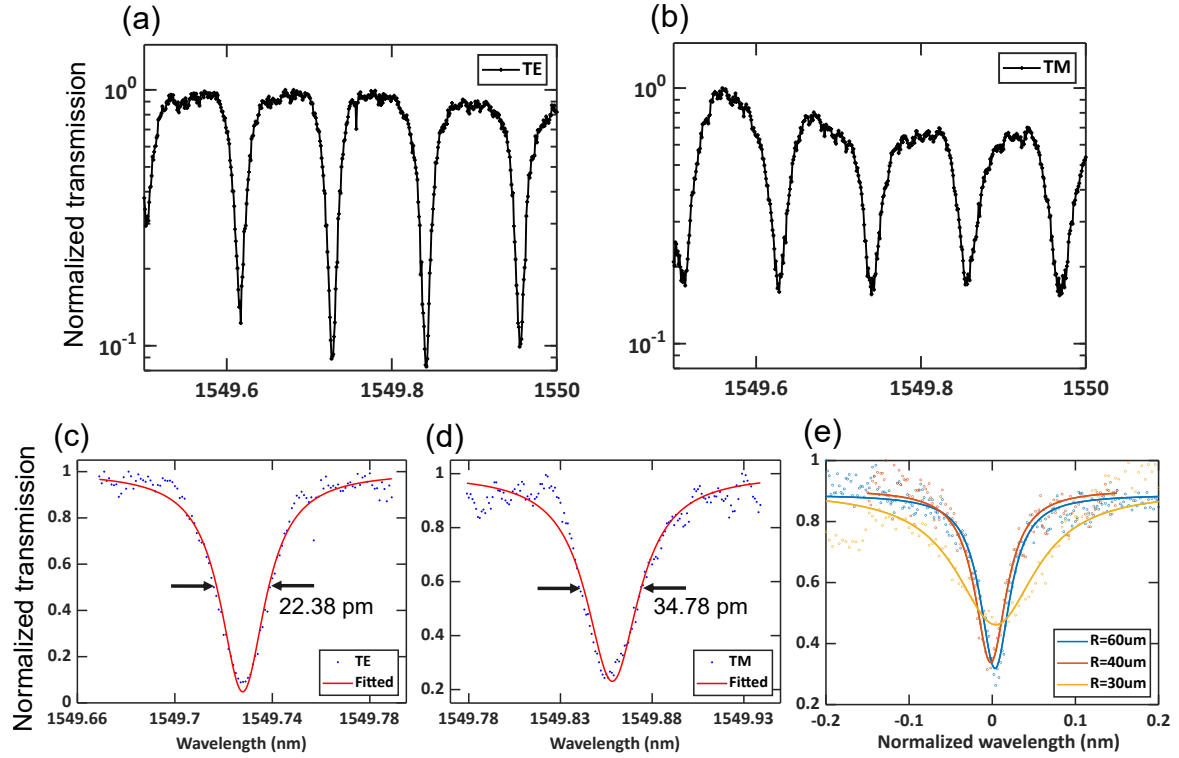


FIG. 3. Characterization of optical properties in the standard waveguide ring resonators: Normalized transmission spectra (dots, log scale) of (a) fundamental TE mode and (b) TM mode. Lorentz fitted resonance dips of (c) TE mode with  $FWHM = 22.38$  pm and (d) TM mode with  $FWHM = 34.78$  pm. (e) Lorentz fitted resonance dips of ring resonators with different bending radii.

### III. DISCUSSION AND CONCLUSION

In conclusion, the a-SiC/LN heterogeneous photonic integrated platform is proposed and realized by a CMOS compatible fabrication processes at a temperature lower than  $165^{\circ}\text{C}$ . Optical ring resonators are characterized and an intrinsic quality factor of  $1.06 \times 10^5$  is measured. Pockels effect is evaluated on this platform by applying an electric field perpendicular to the mode propagation, consequently,  $3.4$  pm/V resonance tunability is achieved in the ring resonator. The applications of this a-SiC/LN platform can be extended to high-speed optical communications, programmable photonics, optical computing, nonlinear optics, and quantum optics. The optical loss can be further improved by optimizing the recipes in fabrication steps including deposition, lithography, etching and annealing. The waveguide dimensions (thickness and width) can be further engineered to significantly reduce the half-wave voltage-length production (for  $260$  nm narrow waveguides  $V_{\pi}L$  is estimated to be  $4.7$  V·cm, reducing a-SiC thickness can possibly push this value lower than  $3$  V·cm). Feed-back loops and active corrections can be implemented to counter the bias point drift induced by long time applied DC-voltage. In principle, the same heterogeneous integration can be applied on bulk lithium niobate substrate as well, utilizing higher nonlinear coefficients and stronger Pockels effect, compared to thin film  $\text{LiNbO}_3$ . Furthermore, the methods developed here and particularly low-temperature ICPCVD a-SiC

constitute a promising route for heterogeneously integration with other ferroelectric substrates, such as barium titanate and lead zirconate titanate. Therefore, with further development and optimization, the demonstrated platform holds great potentials for future heat-free tunable integrated photonics and represents a fundamental building block for second and third-order non-linearities on quantum communication and optical quantum computing.

### ACKNOWLEDGMENTS

The authors acknowledge the valuable comments and suggestions from Silvania. F. Pereira. Z.L. acknowledges the China Scholarship Council (CSC, 202206460012). N.S. and I. E. Z. acknowledge the funding from the NWO OTP COMBO project (project 18757). I. E. Z. acknowledges funding from the European Union's Horizon Europe research and innovation programme under grant agreement No. 101098717 (RESPITE project) and No.101099291 (fastMOT project).

### AUTHOR DECLARATIONS

#### Conflict of Interest

The authors have no conflicts to disclose.

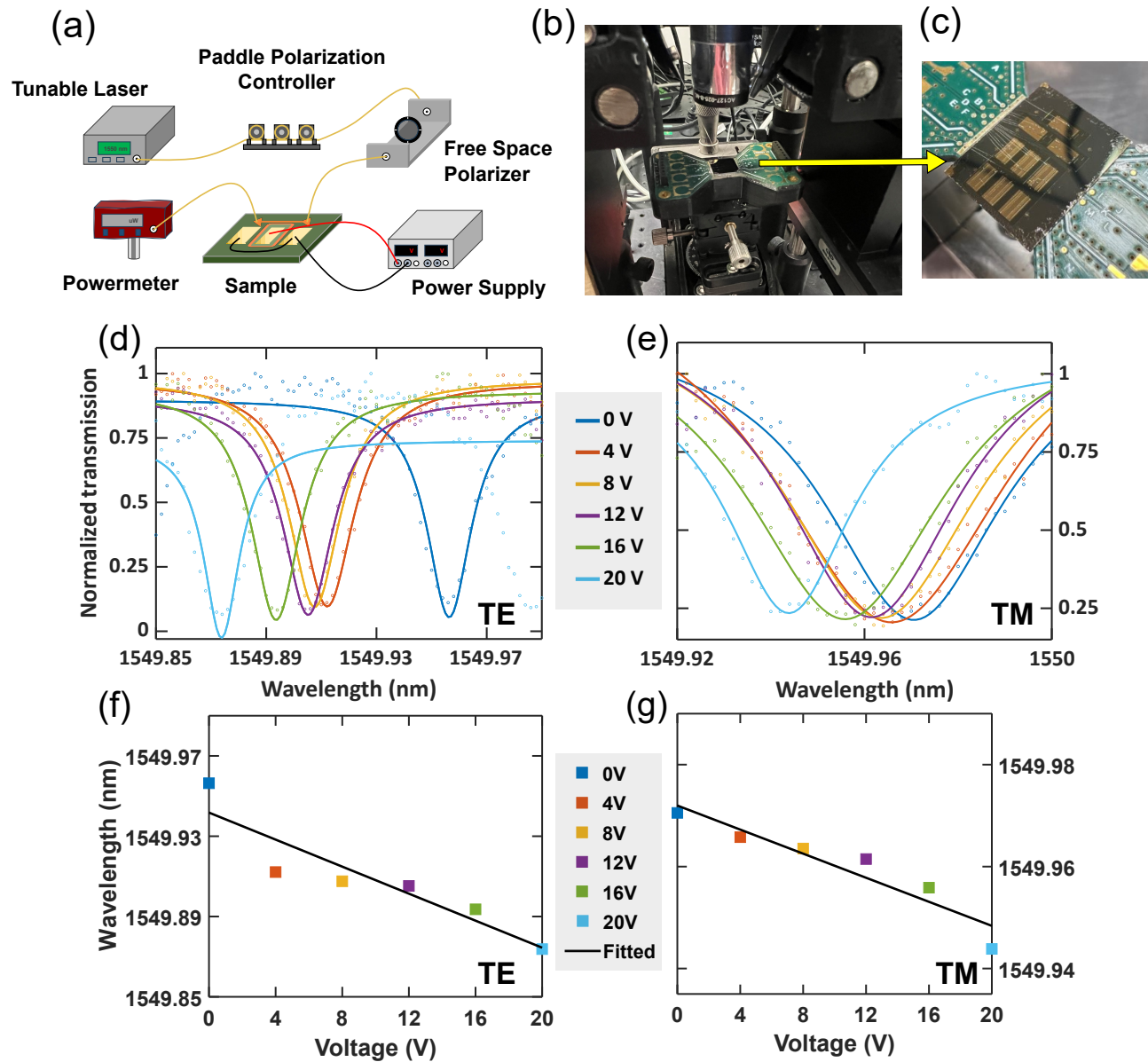


FIG. 4. (a) Schematic diagram and (b) image of the characterization setup. (c) a-SiC/TFLN sample mounted and wire-bonded onto the PCB that connected to the power supply. Normalized transmission spectra of (d) TE mode and (e) TM mode propagated in the ring resonator when DC voltages applied (dots for raw data and solid lines for Lorentzian fittings). Resonance wavelength shifts with respect to DC voltage change (dots) and their linear fittings (solid lines) of (d) TE mode (3.4 pm/V) and (e) TM mode (1.2 pm/V).

#### Author Contributions

**Zizheng Li:** Conceptualization (equal); Data curation (equal); Formal analysis (equal); Investigation (equal); Methodology (equal); Project administration (equal); Software (equal); Supervision (equal); Validation (equal); Visualization (equal); Writing – original draft (equal); Writing – review & editing (equal). **Naresh Sharma:** Conceptualization (equal); Data curation (equal); Formal analysis (equal); Investigation (equal); Supervision (equal); Methodology (equal); Project administration (equal); Software (equal);

Validation (equal); Visualization (equal); Writing – original draft (equal); Writing – review & editing (equal). **Bruno Lopez-Rodriguez:** Conceptualization (equal); Data curation (equal); Formal analysis (equal); Investigation (equal); Methodology (equal); Supervision (equal); Validation (equal); Writing – original draft (equal); Writing – review & editing (equal). **Roald van der Kolk:** Data curation (equal); Formal analysis (equal); Investigation (equal); Methodology (equal); Validation (equal); Writing – original draft (equal); Writing – review & editing (equal). **Thomas Scholte:** Investigation (equal); Data curation (equal); Validation (equal);

Writing – review & editing (equal). **Hugo Voncken:** Data curation (equal); Investigation (equal); Writing – original draft (equal); Writing – review & editing (equal). **Jasper van der Boom:** Data curation (equal); Writing – review & editing (equal). **Simon Gröblacher:** Conceptualization (equal); Supervision (equal); Writing – original draft (equal); Writing – review & editing (equal). **Iman Esmaeil Zadeh:** Conceptualization (equal); Funding acquisition (equal); Conceptualization (equal); Formal analysis (equal); Investigation (equal); Methodology (equal); Project administration (equal); Supervision (equal); Validation (equal); Visualization (equal); Writing – original draft (equal); Writing – review & editing (equal).

## DATA AVAILABILITY

The data that support the findings of this study are available from the corresponding author upon reasonable request.

- <sup>1</sup>A. R. Zanatta, “The optical bandgap of lithium niobate (linbo3) and its dependence with temperature,” *Results in Physics* **39**, 105736 (2022).
- <sup>2</sup>H. Han, L. Cai, and H. Hu, “Optical and structural properties of single-crystal lithium niobate thin film,” *Optical Materials* **42**, 47–51 (2015).
- <sup>3</sup>R. Wu, J. Zhang, N. Yao, W. Fang, L. Qiao, Z. Chai, J. Lin, and Y. Cheng, “Lithium niobate micro-disk resonators of quality factors above 10<sup>7</sup>,” *Optics letters* **43**, 4116–4119 (2018).
- <sup>4</sup>X. Zhu, Y. Hu, S. Lu, H. K. Warner, X. Li, Y. Song, L. Magalhaes, A. Shams-Ansari, N. Sinclair, and M. Loncar, “Twenty-nine million intrinsic q-factor monolithic microresonators on thin film lithium niobate,” arXiv preprint arXiv:2402.16161 (2024).
- <sup>5</sup>R. Zhuang, J. He, Y. Qi, and Y. Li, “High-q thin-film lithium niobate microresonators fabricated with wet etching,” *Advanced Materials* **35**, 2208113 (2023).
- <sup>6</sup>B. Desiatov, A. Shams-Ansari, M. Zhang, C. Wang, and M. Lončar, “Ultra-low-loss integrated visible photonics using thin-film lithium niobate,” *Optica* **6**, 380–384 (2019).
- <sup>7</sup>J. Ma, J. Chen, M. Ren, W. Wu, W. Cai, and J. Xu, “Second-harmonic generation and its nonlinear depolarization from lithium niobate thin films,” *Optics Letters* **45**, 145–148 (2020).
- <sup>8</sup>S. Yuan, Y. Wu, Z. Dang, C. Zeng, X. Qi, G. Guo, X. Ren, and J. Xia, “Strongly enhanced second harmonic generation in a thin film lithium niobate heterostructure cavity,” *Physical Review Letters* **127**, 153901 (2021).
- <sup>9</sup>P.-K. Chen, I. Briggs, C. Cui, L. Zhang, M. Shah, and L. Fan, “Adapted poling to break the nonlinear efficiency limit in nanophotonic lithium niobate waveguides,” *Nature Nanotechnology* **19**, 44–50 (2024).
- <sup>10</sup>C. Wang, M. Zhang, M. Yu, R. Zhu, H. Hu, and M. Loncar, “Monolithic lithium niobate photonic circuits for kerr frequency comb generation and modulation,” *Nature communications* **10**, 978 (2019).
- <sup>11</sup>R. Weis and T. Gaylord, “Lithium niobate: Summary of physical properties and crystal structure,” *Applied Physics A* **37**, 191–203 (1985).
- <sup>12</sup>M. Thomaschewski and S. Bozhevolnyi, “Pockels modulation in integrated nanophotonics,” *Applied Physics Reviews* **9** (2022).
- <sup>13</sup>A. Boes, L. Chang, C. Langrock, M. Yu, M. Zhang, Q. Lin, M. Lončar, M. Fejer, J. Bowers, and A. Mitchell, “Lithium niobate photonics: Unlocking the electromagnetic spectrum,” *Science* **379**, eabj4396 (2023).
- <sup>14</sup>Y. Kong, F. Bo, W. Wang, D. Zheng, H. Liu, G. Zhang, R. Rupp, and J. Xu, “Recent progress in lithium niobate: optical damage, defect simulation, and on-chip devices,” *Advanced Materials* **32**, 1806452 (2020).
- <sup>15</sup>C. Wang, M. Zhang, X. Chen, M. Bertrand, A. Shams-Ansari, S. Chandrasekhar, P. Winzer, and M. Lončar, “Integrated lithium niobate electro-optic modulators operating at cmos-compatible voltages,” *Nature* **562**, 101–104 (2018).
- <sup>16</sup>M. Li, J. Ling, Y. He, U. A. Javid, S. Xue, and Q. Lin, “Lithium niobate photonic-crystal electro-optic modulator,” *Nature Communications* **11**, 4123 (2020).
- <sup>17</sup>M. He, M. Xu, Y. Ren, J. Jian, Z. Ruan, Y. Xu, S. Gao, S. Sun, X. Wen, L. Zhou, *et al.*, “High-performance hybrid silicon and lithium niobate mach-zehnder modulators for 100 gbit s<sup>-1</sup> and beyond,” *Nature photonics* **13**, 359–364 (2019).
- <sup>18</sup>L. Shao, M. Yu, S. Maity, N. Sinclair, L. Zheng, C. Chia, A. Shams-Ansari, C. Wang, M. Zhang, K. Lai, *et al.*, “Microwave-to-optical conversion using lithium niobate thin-film acoustic resonators,” *Optica* **6**, 1498–1505 (2019).
- <sup>19</sup>A. Maeder, G. Finco, F. Kaufmann, A. Sabatti, J. Kellner, R. J. Chapman, and R. Grange, “On-chip tunable quantum interference in a lithium niobate-on-insulator photonic integrated circuit,” *Quantum Science and Technology* **9**, 035040 (2024).
- <sup>20</sup>O. Alibart, V. D’Auria, M. De Micheli, F. Doutre, F. Kaiser, L. Labonté, T. Lunghi, É. Picholle, and S. Tanzilli, “Quantum photonics at telecom wavelengths based on lithium niobate waveguides,” *Journal of Optics* **18**, 104001 (2016).
- <sup>21</sup>R. J. Chapman, S. Häusler, G. Finco, F. Kaufmann, and R. Grange, “Quantum logical controlled-not gate in a lithium niobate-on-insulator photonic quantum walk,” *Quantum Science and Technology* **9**, 015016 (2023).
- <sup>22</sup>X. Wang, X. Jiao, B. Wang, Y. Liu, X.-P. Xie, M.-Y. Zheng, Q. Zhang, and J.-W. Pan, “Quantum frequency conversion and single-photon detection with lithium niobate nanophotonic chips,” *npj Quantum Information* **9**, 38 (2023).
- <sup>23</sup>M. J. Weaver, P. Duivesteyn, A. C. Bernasconi, S. Scharmer, M. Lemang, T. C. v. Thiel, F. Hijazi, B. Hensen, S. Gröblacher, and R. Stockill, “An integrated microwave-to-optics interface for scalable quantum computing,” *Nature Nanotechnology* **19**, 166–172 (2024).
- <sup>24</sup>R. Becker, “Comparison of guided-wave interferometric modulators fabricated on linbo3 via ti indiffusion and proton exchange,” *Applied Physics Letters* **43**, 131–133 (1983).
- <sup>25</sup>G. Chen, N. Li, J. D. Ng, H.-L. Lin, Y. Zhou, Y. H. Fu, L. Y. T. Lee, Y. Yu, A.-Q. Liu, and A. J. Danner, “Advances in lithium niobate photonics: development status and perspectives,” *Advanced Photonics* **4**, 034003–034003 (2022).
- <sup>26</sup>G. R. Paz-Pujalt, D. D. Tuschel, G. Braunstein, T. Blanton, S. T. Lee, and L. M. Salter, “Characterization of proton exchange lithium niobate waveguides,” *Journal of applied physics* **76**, 3981–3987 (1994).
- <sup>27</sup>A. Loni, *An experimental study of proton-exchanged lithium niobate optical waveguides*, Ph.D. thesis, University of Glasgow (1987).
- <sup>28</sup>S. Y. Siew, E. J. H. Cheung, H. Liang, A. Bettiol, N. Toyoda, B. Alshehri, E. Dogheche, and A. J. Danner, “Ultra-low loss ridge waveguides on lithium niobate via argon ion milling and gas clustered ion beam smoothening,” *Optics express* **26**, 4421–4430 (2018).
- <sup>29</sup>Z. Li, R. N. Wang, G. Lihachev, J. Zhang, Z. Tan, M. Churayev, N. Kuznetsov, A. Siddharth, M. J. Beryyhi, J. Riemensberger, *et al.*, “High density lithium niobate photonic integrated circuits,” *Nature Communications* **14**, 4856 (2023).
- <sup>30</sup>X. Huang, Y. Liu, Z. Li, Z. Fan, and W. Han, “High-performance and compact integrated photonics platform based on silicon rich nitride–lithium niobate on insulator,” *APL Photonics* **6** (2021).
- <sup>31</sup>X. Han, M. Yuan, H. Xiao, G. Ren, T. G. Nguyen, A. Boes, Y. Su, A. Mitchell, and Y. Tian, “Integrated photonics on the dielectrically loaded lithium niobate on insulator platform,” *JOSA B* **40**, D26–D37 (2023).
- <sup>32</sup>M. Churayev, R. N. Wang, A. Riedhauser, V. Snigirev, T. Blésin, C. Möhl, M. H. Anderson, A. Siddharth, Y. Popoff, U. Drechsler, *et al.*, “A heterogeneously integrated lithium niobate-on-silicon nitride photonic platform,” *Nature communications* **14**, 3499 (2023).
- <sup>33</sup>M. Thomaschewski, V. A. Zenin, C. Wolff, and S. I. Bozhevolnyi, “Plasmonic monolithic lithium niobate directional coupler switches,” *Nature communications* **11**, 748 (2020).
- <sup>34</sup>T. Ranganath and S. Wang, “Suppression of li2o out-diffusion from ti-diffused linbo3 optical waveguides,” *Applied Physics Letters* **30**, 376–379 (1977).
- <sup>35</sup>G. Poberaj, M. Koechlin, F. Sulser, A. Guarino, J. Hajfler, and P. Günter, “Ion-sliced lithium niobate thin films for active photonic devices,” *Optical materials* **31**, 1054–1058 (2009).
- <sup>36</sup>Y. Jia, L. Wang, and F. Chen, “Ion-cut lithium niobate on insulator technology: Recent advances and perspectives,” *Applied Physics Reviews* **8**, 011307 (2021).
- <sup>37</sup>G. Ulliac, V. Calero, A. Ndao, F. Baida, and M.-P. Bernal, “Argon plasma inductively coupled plasma reactive ion etching study for smooth sidewall



- thin film lithium niobate waveguide application,” *Optical Materials* **53**, 1–5 (2016).
- <sup>38</sup>D. Zhu, L. Shao, M. Yu, R. Cheng, B. Desiatov, C. Xin, Y. Hu, J. Holzgrafe, S. Ghosh, A. Shams-Ansari, *et al.*, “Integrated photonics on thin-film lithium niobate,” *Advances in Optics and Photonics* **13**, 242–352 (2021).
- <sup>39</sup>L. Chen, Q. Xu, M. G. Wood, and R. M. Reano, “Hybrid silicon and lithium niobate electro-optical ring modulator,” *Optica* **1**, 112–118 (2014).
- <sup>40</sup>T. Vandekerckhove, T. Vanackere, J. De Witte, S. Cuyvers, L. Reis, M. Billet, G. Roelkens, S. Clemmen, and B. Kuyken, “Reliable micro-transfer printing method for heterogeneous integration of lithium niobate and semiconductor thin films,” *Optical Materials Express* **13**, 1984–1993 (2023).
- <sup>41</sup>R. Krishna, T. Fan, A. H. Hosseinnia, X. Wu, Z. Peng, and A. Adibi, “Hybrid 3c-silicon carbide-lithium niobate integrated photonic platform,” *Optics Express* **32**, 14555–14564 (2024).
- <sup>42</sup>S. Mookherjee, V. Mere, and F. Valdez, “Thin-film lithium niobate electro-optic modulators: to etch or not to etch,” *Applied Physics Letters* **122** (2023).
- <sup>43</sup>S. Shekhar, W. Bogaerts, L. Chrostowski, J. E. Bowers, M. Hochberg, R. Soref, and B. J. Shastri, “Roadmapping the next generation of silicon photonics,” *Nature Communications* **15**, 751 (2024).
- <sup>44</sup>M. R. Billah, M. Blaicher, T. Hoose, P.-I. Dietrich, P. Marin-Palomo, N. Lindenmann, A. Nestic, A. Hofmann, U. Troppenz, M. Moehle, *et al.*, “Hybrid integration of silicon photonics circuits and inp lasers by photonic wire bonding,” *Optica* **5**, 876–883 (2018).
- <sup>45</sup>T. Vanackere, T. Vandekerckhove, L. Bogaert, M. Billet, S. Poelman, S. Cuyvers, J. Van Kerrebrouck, A. Moerman, O. Caytan, N. Singh, *et al.*, “Heterogeneous integration of a high-speed lithium niobate modulator on silicon nitride using micro-transfer printing,” *APL Photonics* **8** (2023).
- <sup>46</sup>L. Cao, A. Aboketaf, Z. Wang, and S. Preble, “Hybrid amorphous silicon (a-si: H)-linbo<sub>3</sub> electro-optic modulator,” *Optics Communications* **330**, 40–44 (2014).
- <sup>47</sup>L. Chang, Y. Li, N. Volet, L. Wang, J. Peters, and J. E. Bowers, “Thin film wavelength converters for photonic integrated circuits,” *Optica* **3**, 531–535 (2016).
- <sup>48</sup>T. Jin, J. Zhou, and P. T. Lin, “Mid-infrared electro-optical modulation using monolithically integrated titanium dioxide on lithium niobate optical waveguides,” *Scientific Reports* **9**, 15130 (2019).
- <sup>49</sup>H. Nakanishi, H. Nakamura, and R. Goto, “High-electromechanical-coupling-coefficient surface acoustic wave resonator on ta<sub>2</sub>o<sub>5</sub>/al/linbo<sub>3</sub> structure,” *Japanese Journal of Applied Physics* **49**, 07HD21 (2010).
- <sup>50</sup>P. Rabiei, J. Ma, S. Khan, J. Chiles, and S. Fathpour, “Heterogeneous lithium niobate photonics on silicon substrates,” *Optics express* **21**, 25573–25581 (2013).
- <sup>51</sup>B. Lopez-Rodriguez, R. Van Der Kolk, S. Aggarwal, N. Sharma, Z. Li, D. Van Der Plaats, T. Scholte, J. Chang, S. Groblacher, S. F. Pereira, *et al.*, “High-quality amorphous silicon carbide for hybrid photonic integration deposited at a low temperature,” *ACS photonics* **10**, 3748–3754 (2023).
- <sup>52</sup>D. M. Lukin, M. A. Guidry, and J. Vučković, “Integrated quantum photonics with silicon carbide: challenges and prospects,” *PRX quantum* **1**, 020102 (2020).
- <sup>53</sup>S. Castelletto, A. Peruzzo, C. Bonato, B. C. Johnson, M. Radulaski, H. Ou, F. Kaiser, and J. Wrachtrup, “Silicon carbide photonics bridging quantum technology,” *ACS Photonics* **9**, 1434–1457 (2022).
- <sup>54</sup>D. M. Lukin, C. Dory, M. A. Guidry, K. Y. Yang, S. D. Mishra, R. Trivedi, M. Radulaski, S. Sun, D. Verduyck, G. H. Ahn, *et al.*, “4h-silicon-carbide-on-insulator for integrated quantum and nonlinear photonics,” *Nature Photonics* **14**, 330–334 (2020).
- <sup>55</sup>P. Xing, D. Ma, L. C. Kimerling, A. M. Agarwal, and D. T. Tan, “High efficiency four wave mixing and optical bistability in amorphous silicon carbide ring resonators,” *APL Photonics* **5** (2020).
- <sup>56</sup>P. Xing, D. Ma, K. J. Ooi, J. W. Choi, A. M. Agarwal, and D. Tan, “Cmos-compatible pecvd silicon carbide platform for linear and nonlinear optics,” *ACS Photonics* **6**, 1162–1167 (2019).
- <sup>57</sup>L.-Y. S. Chang, H. Nejadriahi, S. Pappert, and P. K. Yu, “Demonstration of dc kerr effect induced high nonlinear susceptibility in silicon rich amorphous silicon carbide,” *Applied Physics Letters* **120** (2022).
- <sup>58</sup>I. E. Zadeh, A. W. Elshaari, K. D. Jons, A. Fognini, D. Dalacu, P. J. Poole, M. E. Reimer, and V. Zwiller, “Deterministic integration of single photon sources in silicon based photonic circuits,” *Nano letters* **16**, 2289–2294 (2016).
- <sup>59</sup>C. Cushman, N. Smith, M. Kaykhaii, N. Podraza, and M. Linford, “An introduction to modeling in spectroscopic ellipsometry, focusing on models for transparent materials: The cauchy and sellmeier models,” *Vacuum Technology & Coating* **7** (2016).
- <sup>60</sup>J. P. Salvestrini, L. Guilbert, M. Fontana, M. Abarkan, and S. Gille, “Analysis and control of the dc drift in linbo<sub>3</sub>-based mach-zehnder modulators,” *Journal of lightwave technology* **29**, 1522–1534 (2011).
- <sup>61</sup>H. Nagata, N. O’Brien, W. Bosenberg, G. Reiff, and K. Voisine, “De-voltage-induced thermal shift of bias point in linbo<sub>3</sub>/sub 3/optical modulators,” *IEEE photonics technology letters* **16**, 2460–2462 (2004).
- <sup>62</sup>S. Sun, M. He, M. Xu, S. Gao, Z. Chen, X. Zhang, Z. Ruan, X. Wu, L. Zhou, L. Liu, *et al.*, “Bias-drift-free mach-zehnder modulators based on a heterogeneous silicon and lithium niobate platform,” *Photonics Research* **8**, 1958–1963 (2020).